Electromagnetic simulations for the He6-CRES RF system

Luciano Malavasi
Department of Physics, Worcester Polytechnic Institute
Department of Physics, University of Washington (Physics REU 2023)

Alejandro García and Nicholas Buzinsky
Department of Physics, University of Washington
(Dated: September 14, 2023)

The sensitivity of the He6-CRES experiment is limited by frequency-dependent oscillations in the signal-to-noise ratio (SNR) observed in initial data. We model these oscillations as a result of various reflective components in the apparatus forming a multi-mirror Fabry-Pérot cavity. This paper analyzes this effect using both traditional optical methods and cascaded scattering parameters. We also characterize several elements of our radio-frequency (RF) system, namely the quarter-wave polarizer and circular-to-rectangular waveguide transition. Electromagnetic simulations of key RF components along with a model for the reflections will allow us to mitigate the issue of irregular SNR.

I. INTRODUCTION

The He6-CRES experiment is a nuclear physics experiment that will perform high-precision β-decay spectroscopy of ^{6}He and ^{19}Ne through a novel frequency-based experimental technique called Cyclotron Radiation Emission Spectroscopy (CRES) [1]. The experiment is a low-energy probe of physics Beyond the Standard Model, as distortions to the β spectrum may correspond to non-standard scalar and tensor couplings, parametrized by the Fierz interference term b_{Fierz} [2].

A. Cyclotron Resonance Emission Spectroscopy

A particle with charge q and mass m (e.g. electron or positron, denoted $\beta^{\pm}$) in a magnetic field $\vec{B}$ undergoes cyclotron resonance,

$$q\vec{v} \times \vec{B} = \gamma \frac{mv^2}{r}. \tag{1}$$

Taking $E = \gamma mc^2$, the frequency of cyclotron resonance f_c for a $\beta^{\pm}$ with energy E is given by

$$f_c = \frac{|q|}{2\pi} \frac{Bc^2}{E}. \tag{2}$$

The frequency of cyclotron resonance depends inversely on E. Measuring f_c is thus a proxy for measuring the energy of a $\beta^{\pm}$ particle without directly interacting with it [3]. As a charged particle spins, it emits coherent circularly polarized electromagnetic radiation at the cyclotron frequency, which couple to the fundamental mode of a circular waveguide and are received by an antenna and amplified. The cyclotron frequency increases as the particle loses energy to radiation, so CRES events appear as chirped signals at the LNA output.

CRES was pioneered by the Project 8 collaboration to measure the neutrino mass via the tritium β spectrum endpoint (18.6 keV) [3, 4], as a low-volume alternative to other precision β spectroscopy experiments such as KATRIN [5]. The He6-CRES experiment applies CRES over a much broader energy bandwidth, to measure full β spectra rather than just the region around the endpoint.

CRES has various advantages compared to traditional β calorimetry methods. Experiments that involve depositing energy in a semiconductor or scintillator detector must account for losses such as backscattering and bremsstrahlung, and energy resolution is limited by the detector material. CRES does not directly measure β interactions with matter, and energy resolution is fixed by the frequency resolution of the Fourier transform applied to the amplifier readout [1].

B. He6-CRES RF system

A diagram of the Phase II He6-CRES RF system is given in Figure 1. CRES events occur in the decay cell (**A**), which contains the gaseous β emitter. CRES radiation leaves the decay cell and passes through a circular-to-linear polarizer (**B**). The linearly polarized wave passes through a waveguide transition (**C**) to a rectangular waveguide (**D**), to RF low-noise amplifiers (LNAs) (**E**). CRES radiation leaving the decay cell in the opposite direction propagates through a circular waveguide to a waveguide terminator (**F**).

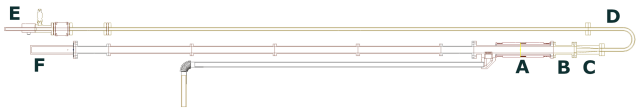

FIG. 1: Diagram of He6-CRES system. **A**: Decay cell. **B**: Polarizer. **C**: circular-to-rectangular waveguide transition. **D**: Rectangular waveguide. **E**: to LNAs. **F**: circular waveguide terminator.

In the previous iteration of the experiment (Phase I), the two sides of the decay cell had symmetric RF systems

apart from the waveguide U-bend. Instead of a terminator at **F**, a second RF amplifier system read CRES data in parallel to the readout at **E**.

The amplifier readout is digitized at 2400 MHz in bins of 2^{13} samples. The Fourier transform of the binned data forms a 2D plot of Fourier amplitude in frequency and time.

C. Observed SNR oscillations

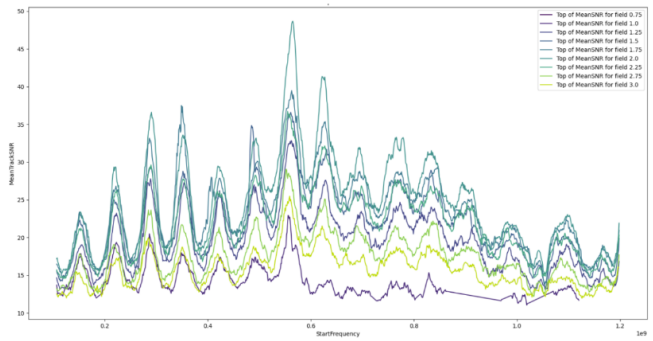

FIG. 2: SNR vs. frequency varying magnetic field strength, before installing terminator

In the intial He6-CRES data collection stage (Phase I), we observed a strong frequency-dependent oscillations in the signal-to-noise ratio (SNR), as shown in Figure 2 at various B-field strengths. These oscillations are characteristic of internal reflections of CRES radiation off of various components in the RF assembly causing constructive and destructive interference of the signal. The waveguide terminator at point F of Figure 1 was installed to mitigate these reflections, but the SNR oscillations remained a prominent feature of the experimental data (Fig. 3). SNR variations interfere with accurate CRES event reconstruction, limiting our sensitivity to b_{Fierz}. It is therefore critical for the experiment to exhibit uniform and sufficiently high SNR over the frequency range of interest, and efforts to understand, characterize, and correct this issue are underway.

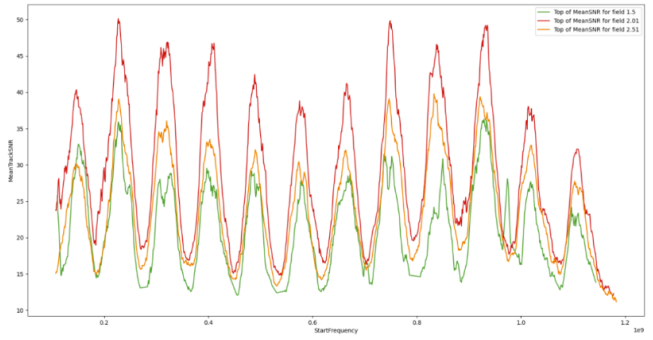

FIG. 3: SNR vs. frequency varying magnetic field strength, with terminator

II. THEORY OF WAVEGUIDES

A plane wave propagating losslessly along the z-axis has a harmonic time and z dependence as $e^{i(\omega t-\beta z)}$, where the propagation constant $\beta = \frac{2\pi}{\lambda} = \frac{\omega}{v_p}$, carrying a wave number $k = \frac{2\pi}{\lambda_0} = \frac{\omega}{c}$, where λ is the physical (peak-to-peak) wavelength, v_p is the phase velocity, λ_0 is the free-space wavelength of a plane wave with frequency ω, and $c = \frac{1}{\sqrt{\varepsilon\mu}}$ [6]. Representing the wave as a phasor and omitting the time-dependent term, the phase of the wave is $\phi(z) = \beta z$, and the phase shift picked up over a distance of L is accordingly $\phi = \beta L$.

In a TEM structure (e.g. coplanar waveguide or free space), $\beta = k$. For TE or TM waves, as in circular and rectangular waveguides, this simplifying relationship does not hold, instead propagation is described by the cutoff wavelength k_c, such that [6]

$$k_c^2 = k^2 - \beta^2. \tag{3}$$

To support $e^{i\beta z}$ propagation through a waveguide, it is required that β be real, equivalently

$$\beta^2 = k^2 - k_c^2 > 0. \tag{4}$$

k_c is determined by solving Maxwell's Equations inside the specific geometry of the waveguide, and depends on the waveguide dimension mode indices (n, m). With R as the inner radius of the circular waveguide, a and b as the inner dimensions of the rectangular waveguide along x and y respectively, [6]

$$k_c = \sqrt{\left(\frac{n\pi}{a}\right)^2 + \left(\frac{m\pi}{b}\right)^2} \text{ (rectangular waveguide)} \tag{5}$$

$$k_c = \frac{p_{nm}}{R} \text{ (circular waveguide, TM}_{nm}\text{)} \tag{6}$$

$$k_c = \frac{p'_{nm}}{R} \text{ (circular waveguide, TE}_{nm}\text{)}. \tag{7}$$

Here, p_{nm} and p'_{nm} denote the mth zero of the Bessel function of the first kind $J_n(x)$ and its derivative $J'_n(x)$.

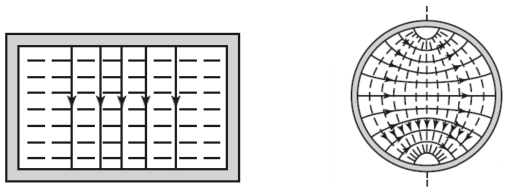

(a) (b)

FIG. 4: Cross section of TE_{10} in a rectangular waveguide (a) and TE_{11} in a circular waveguide, polarized along x (b) [7]

The fundamental mode of a waveguide is the mode with the lowest cutoff wave number. In a rectangular

waveguide, the fundamental mode is (taking $a > b$ without loss of generality) the TE_{10} mode, with $k_c = \frac{\pi}{a}$ (Fig. 4a). In a circular waveguide, this is the TE_{11} mode, with $k_c \approx \frac{1.8412}{R}$, depicted in Figure 4b. This mode is degenerate with continuous polar symmetry, so it is conventionally analyzed as two orthogonal polarizations along x and y.

III. MODELING MULTI-PATH PROPAGATION

The observed SNR oscillations can be explained as evidence of multi-path propagation due to reflections inside the RF system. At any reflective interface inside the system, some of the signal is transmitted and some is reflected. With multiple reflective interfaces, the signal may reflect internally an arbitrary number of times, interfering with other signals inside the cavity and creating frequency-selective effects similar to what we observe.

A. Fabry-Pérot interferometer

A well-known example of the frequency selection effect in multi-path propagation is a Fabry-Pérot interferometer, constructed with two thin parallel mirrors forming an optical cavity. Light can only escape this cavity when it is in resonance with the cavity, which occurs when the transmitted and reflected waves are in phase and constructively interfere.

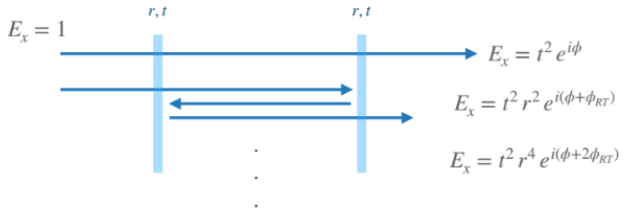

FIG. 5: A diagram of a Fabry-Pérot cavity, including the 0th, 1st, and 2nd order reflections [8]. $\phi_{RT} = 2\phi$.

We can directly analyze the transmission through a 2-mirror Fabry-Pérot cavity in terms of the coefficient of reflection r and transmission t of the mirrors, which denote the proportion of the incident field amplitude that is reflected or transmitted at the mirror. We may express the separation of the mirrors in terms of the phase ϕ picked up by a wave traveling from one to the other, with implicit frequency dependence.

To zeroth order, a wave transmits through the first mirror, travels to the second mirror, and transmits through, transforming by a factor of $T_0 = t^2 e^{i\phi}$. In the first order reflection, the wave reflects at the second mirror, reflects at the first mirror, and then transmits out, for a total transmission factor of $T_1 = t^2 r^2 e^{i3\phi}$. The n-th order reflection transmits through both mirrors and makes n round-trip reflections for a transmission factor of $T_n = t^2 r^{2n} e^{i\phi(1+2n)}$. The overall transmission factor, summing over all reflection orders, is thus a geometric series

$$E_x = t^2 e^{i\phi} \sum_{n=0}^{\infty} r^{2n} e^{i2n\phi} = \frac{t^2 e^{i\phi}}{1 - r^2 e^{i2\phi}}. \tag{8}$$

B. Multi-path reflection as a Markov chain

Extending the previously detailed analysis beyond the standard 2-mirror case to $N > 2$ mirrors proves challenging due to the combinatorial explosion of possible paths light can take through the system. Instead, we can model the optical cavity by borrowing from the theory of Markov chains [9].

A Markov chain is a stochastic process formed of discrete states, where the probability of transitioning to any state only depends on the current state. Markov chains may be represented graphically as a state diagram, or numerically as a square matrix R, where R_{ij} represents the transition probability from state i to state j. Furthermore, $(R^k)_{ij}$ represents the transition probability from state i to j after k steps.

To construct a Markov chain representing an optical cavity, we may consider a wave inside the apparatus as existing in one of a finite number of states, enumerated by region in the system and direction of propagation. Instead of probabilities between the states, we may instead express the amplitude and phase ratio between these states in terms of r, t, and ϕ. As a simple example, a 2-mirror Fabry-Pérot cavity can be represented with the Markov chain shown in Figure 6, along with its corresponding transition matrix.

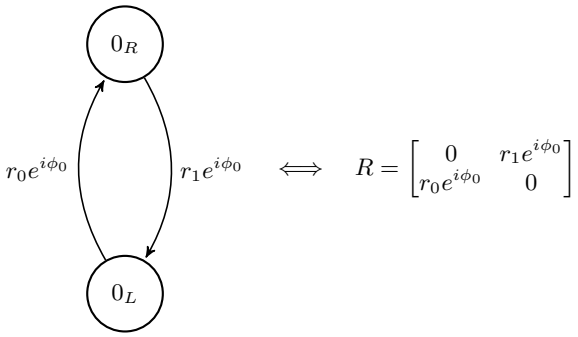

FIG. 6: Markov chain representing a 2-mirror Fabry-Pérot cavity [9].

The total wave amplitude in each state in the system is expressed in the fundamental matrix of the Markov chain F, denoting the overall transition probability (here, amplitude) between any two states. It is derived by evaluating the following Neumann series, in close analogy to

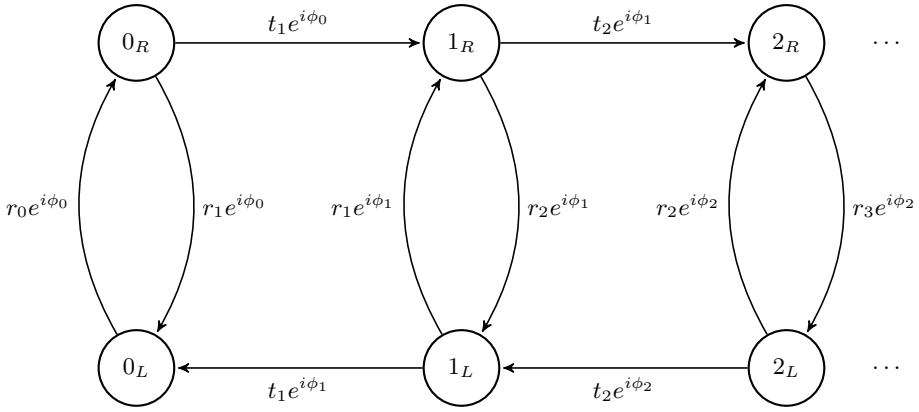

FIG. 7: Markov model for a N-mirror Fabry-Pérot Cavity. The first 3 regions (corresponding to 4 mirrors) are shown. Note the traditional 2-mirror Fabry-Pérot Cavity is a subset ($\{0_R, 0_L\}$) of this larger diagram [9].

a geometric series [10]

$$F = \sum_{k=0}^{\infty} R^k = (\mathbf{I} - R)^{-1}. \tag{9}$$

This sum necessarily converges since $|R_{ij}| < 1$.
The fundamental matrix follows simply from (9).

$$T = (\mathbf{I} - R)^{-1} = \frac{1}{1 - r_0 r_1 e^{i2\phi_0}} \begin{bmatrix} 1 & r_0 e^{i\phi_0} \\ r_1 e^{i\phi_0} & 1 \end{bmatrix} \tag{10}$$

The proportion of the incident signal that ultimately leaves the cavity is the total amount in the 0_R state $T_{0,0}$ times the phase and amplitude picked up by transmission through each mirror. Taking $r^2 = r_0 r_1$, we recover Equation 8 exactly. Unlike before, this analysis extends naturally to $N > 2$ mirror systems, by constructing Markov chains similar to Figure 7. Additional model parameters, for example polarization-dependent behavior, can be included simply by extending the chain with additional states with appropriate transition factors.

C. Scattering parameters

Scattering parameters (S-parameters) are a type of linear network parameter that relate the amplitudes of incident and reflected waves at each port of a microwave network. S-parameters describe how much a wave incident on any one port excites a wave leaving a specific port. By using field amplitudes, S-parameters bypass the ambiguity of defining voltage and current in non-TEM structures, and lend themselves especially well to analysis of components at microwave frequencies.

A typical 2-port microwave network is depicted in Figure 8.

The S-parameters for a 2-port network are defined as:

$$\begin{pmatrix} b_1 \\ b_2 \end{pmatrix} = \begin{bmatrix} S_{11} & S_{12} \\ S_{21} & S_{22} \end{bmatrix} \begin{pmatrix} a_1 \\ a_2 \end{pmatrix} \tag{11}$$

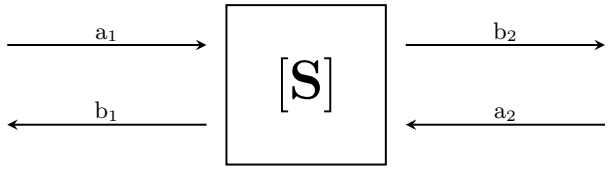

FIG. 8: 2-port S-parameters, with incident and reflected field amplitudes a_n and b_n

In the canonical 2-port example, $S_{11} = \frac{b_1}{a_1}|_{a_2=0}$ is the reflection at port 1 when port 2 is terminated, and $S_{21} = \frac{b_2}{a_1}|_{a_2=0}$ is the transmission from port 1 to port 2 when port 2 is terminated.

A general N-port network can be described by the following S-parameter matrix. Generally, S_{ij} expresses how much a signal incident on port j excites a wave at port i, when all ports other than j have zero incident signal.

$$\begin{pmatrix} b_1 \\ \vdots \\ b_n \end{pmatrix} = \begin{pmatrix} S_{11} & \dots & S_{1n} \\ \vdots & \ddots & \vdots \\ S_{n1} & \dots & S_{nn} \end{pmatrix} \begin{pmatrix} a_1 \\ \vdots \\ a_n \end{pmatrix} \tag{12}$$

D. Transfer scattering parameters

Transfer scattering paramaters, or T-parameters, are another wave-amplitude network parameter that allow for characterizing the overall performance of several "cascaded" microwave networks in series [7]. T-parameters allow for cascading microwave networks in close analogy to using ABCD network parameters for cascading 2-port lumped element networks. For a two-port network, the T-parameters are defined as

$$\begin{pmatrix} b_1 \\ a_1 \end{pmatrix} = \begin{bmatrix} T_{11} & T_{12} \\ T_{21} & T_{22} \end{bmatrix} \begin{pmatrix} a_2 \\ b_2 \end{pmatrix} \tag{13}$$

Consider two two-port networks with T-parameters T_1 and T_2. The T-parameter matrix describing the series

combination of the two networks is simply $T = T_1 T_2$, and this cascading extends to an arbitrary number of networks in series. Most importantly, while T-parameters cannot be physically measured in the same way as S-parameters, there exists a well-known conversion between S-parameters and T-parameters [7],

$$\begin{aligned} T_{11} &= S_{12} - \frac{S_{11}}{S_{22}} S_{21} & S_{11} &= \frac{T_{12}}{T_{22}} \\ T_{12} &= \frac{S_{11}}{S_{21}} & S_{12} &= T_{11} - \frac{T_{12} T_{21}}{T_{22}} \\ T_{21} &= -\frac{S_{22}}{S_{21}} & S_{21} &= \frac{1}{T_{22}} \\ T_{22} &= \frac{1}{S_{21}} & S_{22} &= -\frac{T_{21}}{T_{22}} \end{aligned} \tag{14}$$

Using these conversions, we can obtain "overall" S-parameters of a series of cascaded microwave networks with known S-parameters $S_1, \ldots, S_N$ by following a simple algorithm:

1. Using S to T transformations from (14), convert each $S_1, \ldots, S_N$ to T-parameters $T_1, \ldots, T_N$.
2. Calculate the overall T parameter of the entire network with simple matrix multiplication
$$T = \prod_n T_n.$$
3. Using T to S transformations from (14), convert T to the overall network S parameters.

This overall S-parameter matrix takes into account the full wave behavior throughout the whole network naturally from the T-parameter chaining, without additional analysis needed.

E. Generalizing T-parameters to N-port networks

Recent studies [11, 12] explore the idea of generalizing the traditional two-port T-parameter definition to a cascaded series networks with $N > 2$. The S-parameter matrix of an N-port network remains square ($N \times N$) for all N. The definition of the T-parameters implicitly requires denoting ports as input ("external") ports or output ("internal") ports for chaining, so in unbalanced networks with a different number of internal and external ports the input/output symmetry is broken [11]. An unbalanced network with will thus have a non-square T-matrix. However, balanced networks still have a square T-parameter matrix, and we will limit the scope of this discussion to balanced 4-port networks, with two external ports and two internal ports. The T-parameter matrix for such a network with external ports 1,2 and internal ports 3,4 is

$$\begin{pmatrix} b_1 \\ b_2 \\ a_1 \\ a_2 \end{pmatrix} = \begin{bmatrix} T_{11} & T_{12} & T_{13} & T_{14} \\ T_{21} & T_{22} & T_{23} & T_{24} \\ T_{31} & T_{32} & T_{33} & T_{34} \\ T_{41} & T_{42} & T_{43} & T_{44} \end{bmatrix} \begin{pmatrix} a_3 \\ a_4 \\ b_3 \\ b_4 \end{pmatrix} \tag{15}$$

Cascading 3 such networks is schematically represented in Figure 9.

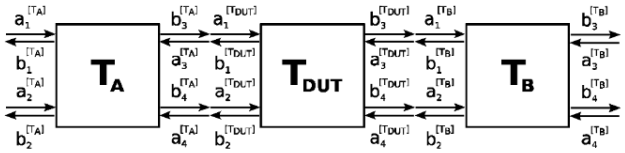

FIG. 9: Cascading three 4-port balanced networks with T-parameters [11]

Working with ports assigned as external or internal, N-port network parameters may be either between two external ports (external-to-external), between two internal ports (internal-to-internal), internal-to-external, or external-to-internal. Notice that a multiport network parameter matrix can be decomposed into submatrices of parameters that fall in the same "group" of input and output ports, as in (16).

$$S = \begin{bmatrix} [S_{ee}] & [S_{ei}] \\ [S_{ie}] & [S_{ii}] \end{bmatrix} \qquad T = \begin{bmatrix} [T_{ee}] & [T_{ei}] \\ [T_{ie}] & [T_{ii}] \end{bmatrix} \tag{16}$$

It can be shown [11, 12] that not only does a transformation between N-port S- and T-parameters exist, it generally preserves much of the familiar structure of (14).

$$\begin{aligned} T_{11} &= S_{ei} - S_{ee} S_{ie}^{-1} S_{ii} & S_{ee} &= T_{ei} T_{ii}^{-1} \\ T_{12} &= S_{ee} S_{ie}^{-1} & S_{12} &= T_{ee} - T_{ei} T_{ii}^{-1} T_{ie} \\ T_{21} &= -S_{ie}^{-1} S_{ii} & S_{21} &= T_{ii}^{-1} \\ T_{22} &= S_{ie}^{-1} & S_{22} &= -T_{ii}^{-1} T_{ie} \end{aligned} \tag{17}$$

This is an appealing formalism for analyzing RF elements in the He6-CRES experiment. The fundamental mode of a circular waveguide is the TE_{11} mode, which is degenerate with polar symmetry. We decompose this mode into orthogonal x and y polarizations, which can be treated as two independent "virtual" ports at the same "physical" port. In this sense, a two-ended component in a circular waveguide can be analyzed as a balanced 4-port network.

IV. HFSS SIMULATION OF RF COMPONENTS

Full-wave simulations of the RF components were performed in Ansys HFSS, a finite-element method solver for full-wave electromagnetic simulations. The geometries of various components were modeled and assigned material properties. The waveguide structure enclosing each component was assigned wave-port excitations at either end, which instructs HFSS to numerically solve for the modes of the waveguide in order of increasing cutoff frequency, then to express the S-parameters of the structure in terms of the waveguide modes at the port. Ansys HFSS reports S-parameters for each mode of each physical port of the

structure being simulated. For legibility, this document attempts to retain the familiar two-port language (S_{11}, S_{12}, S_{21}, and S_{22}) with an additional qualifier for the polariztion of the mode in question, rather than use 4-port notation.

A. Circular-to-linear polarizer

The quarter-wave polarizer applies a 90° relative phase shift between orthogonal components of a wave at 45° relative to the orientation of the polarizer. This allows for the conversion of circularly polarized waves to linearly polarized waves as well as the reverse. Traditionally, this polarization is performed with a birefringent crystal [13], but the He6-CRES polarizer is a diamond-shaped dielectric sheet inside a circular waveguide (diameter 0.455"), for improved broadband performance (Fig. 10).

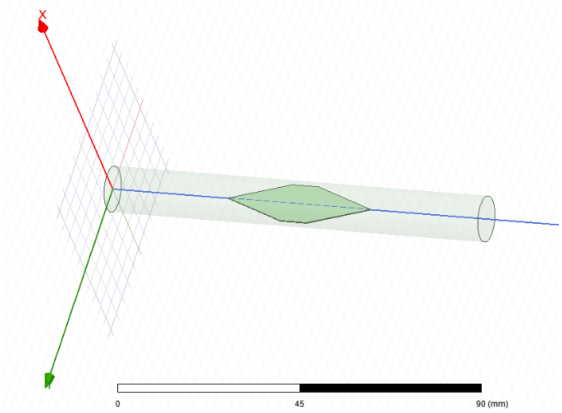

FIG. 10: Polarizer model in HFSS

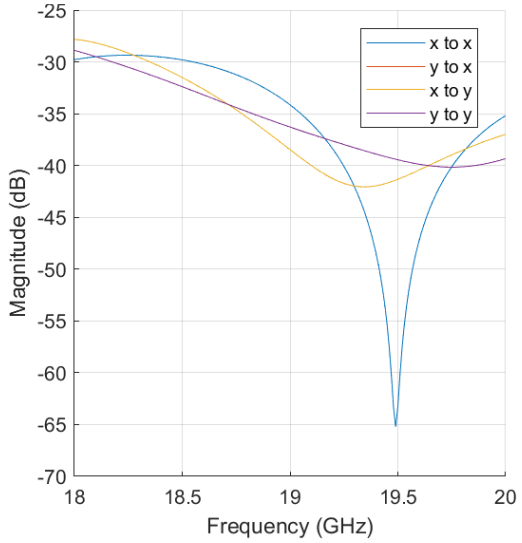

FIG. 11: Polarizer input reflection (S_{11}, all TE_{11} polarizations)

In simulation, S_{11} is below -25 dB for both modes and cross-mode excitations. There is slight asymmetry between the x-polarized and y-polarized modes, notably in a resonance at around 19.5 GHz in the reflection from the x-polarized mode into itself (Fig. 11).

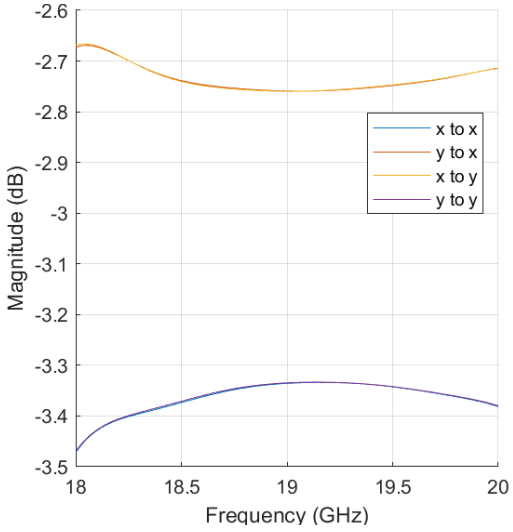

FIG. 12: Polarizer transmission (S_{21}, all TE_{11} polarizations)

Simulated S_{21} of the polarizer is near -3 dB for all polarizations, corresponding to half-power transmission (Fig. 12). This makes sense: a linearly polarized wave is converted to a circularly polarized wave, a superposition of two orthogonally polarized waves. Half the power of a wave transmits as a component polarized along x, and half transmits polarized along y. There is a slight asymmetry due to imperfect polarization: about -2.8 to -2.65 dB is transmitted across polarizations, while -3.5 to -3.3 dB transmits in the original polarization.

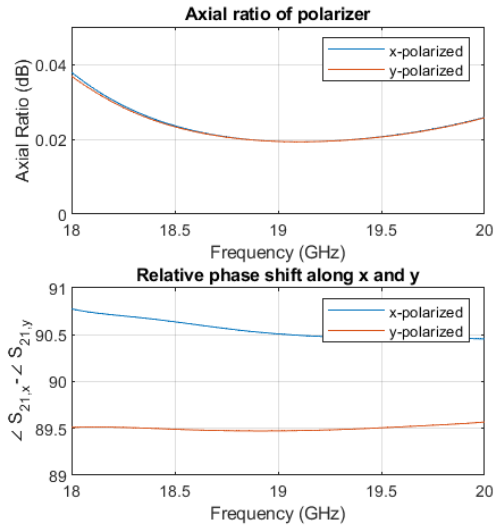

FIG. 13: Polarizer axial ratio and relative phase shift

Another important figure of merit in studying the quality of elliptical polarization is the axial ratio, the ratio between the major and minor axis amplitudes of an elliptically polarized wave. Perfect circular polarization has an axial ratio of 0 dB, and by convention a practical circularly polarized wave is understood to have an axial ratio < 3 dB. Additionally, we plot the phase difference between S_{21} to both x- and y-polarized modes from either polarization at the input.

We observe an excellent axial ratio < 0.04 dB across our frequency range of interest. The relative phase shift between x and y components of a wave is within 1° of 90° for both x- and y-polarized incident waves.

B. Circular-to-rectangular waveguide transition

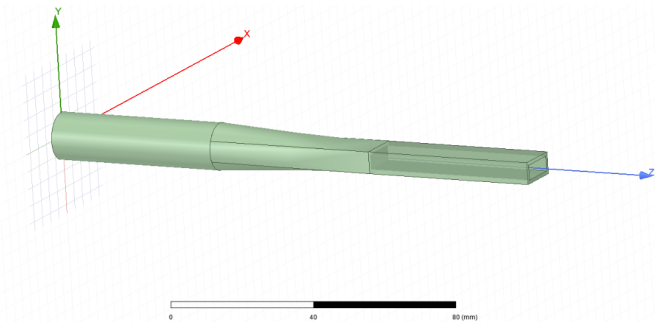

FIG. 14: Circular-to-rectangular transition model in HFSS. Input at circular port, output at rectangular port.

The circular-to-rectangular transition ("taper") is a continuous deformation from a circular waveguide to a WR-42 rectangular waveguide. Notably, only the fundamental TE_{01} mode of a rectangular WR-42 waveguide has a cutoff frequency below our frequency range of interest, at 14.05 GHz. The next mode, TE_{02}, has a cutoff frequency of 28.10 GHz. The TE_{01} mode has a cutoff frequency of 34.71 GHz, and is of more interest than the TE_{02} mode as it is orthogonal to the TE_{01}. Components of a wave that project onto non-propagating modes reflect, so this taper is of interest as the first obvious location where high reflection may occur the apparatus.

The model (Fig. 14) is oriented so the E-field of the propagating TE_{10} is parallel to the y-axis. We anticipate an incident wave linearly polarized along y to transmit. The non-propagating TE_{01} mode has an E-field parallel to x, so x-polarized waves are expected to reflect. We can quantitatively observe this behavior in the reflection (Fig. 15) and transmission (Fig. 16) characteristics.

We see nearly perfect reflection of x-polarized waves at the circular input, and very little reflection of y-polarized waves, between -40 and -30 dB. Reflection from either polarization into the other is less than -38 dB with equal magnitude from x to y as from y to x.

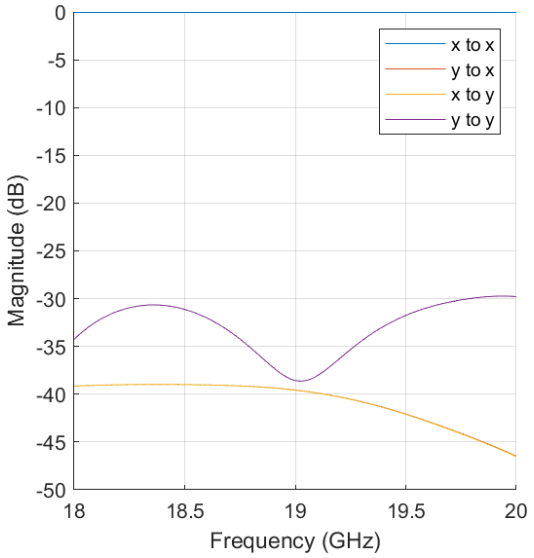

FIG. 15: Taper input reflection (S_{11}, all TE_{11} polarizations).

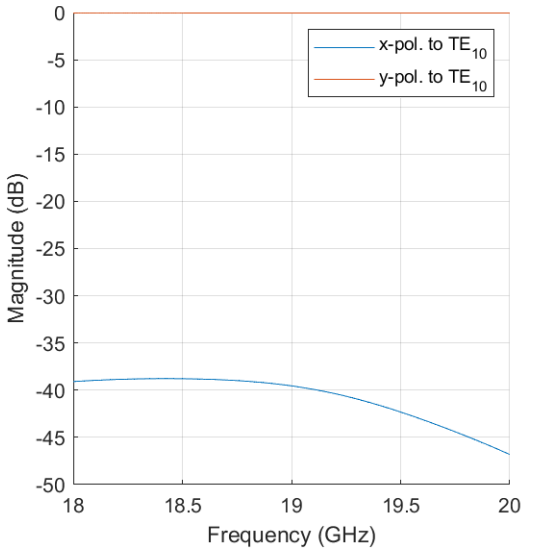

FIG. 16: Taper transmission (S_{21} to rectangular TE_{10})

Similarly, in Figure 16 we observe nearly perfect transmission (0 dB) from the y-polarized TE_{11} mode to the propagating mode of the rectangular wave guide, but the x-polarized mode does not transmit, with $S_{21} < -38$ dB. S_{21} from either input polarization into the non-propagating mode is omitted.

V. CASCADING POLARIZER AND TAPER

The polarizer and circular-to-rectangular taper are in series in the He6-CRES experiment and act as a larger "unit" whose behavior is important to characterize. We can also characterize the behavior of these components

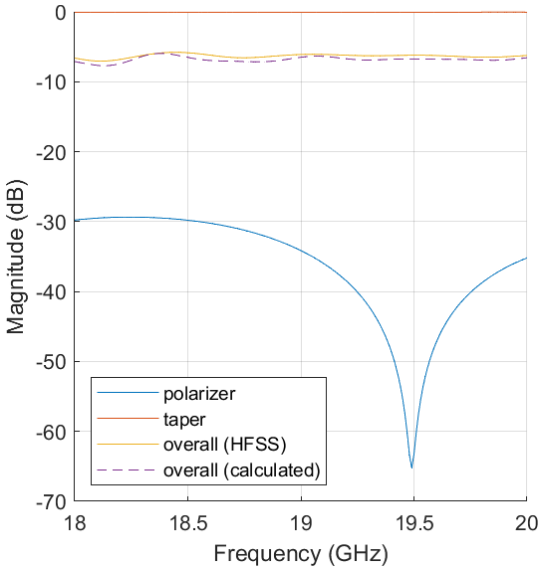

(a) x-polarized mode

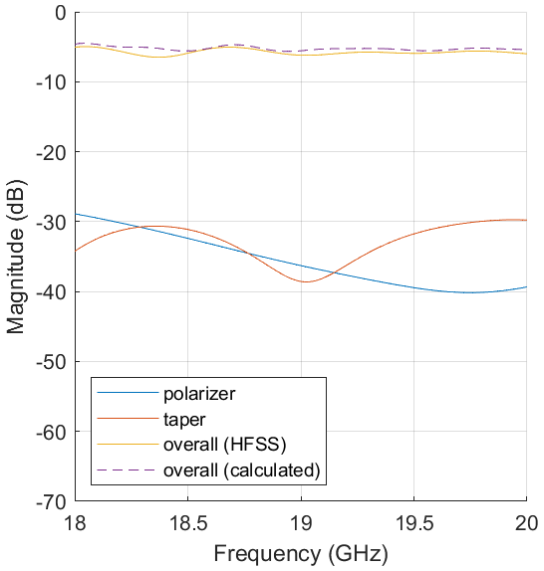

(b) y-polarized mode

FIG. 17: S_{11} of both components in series

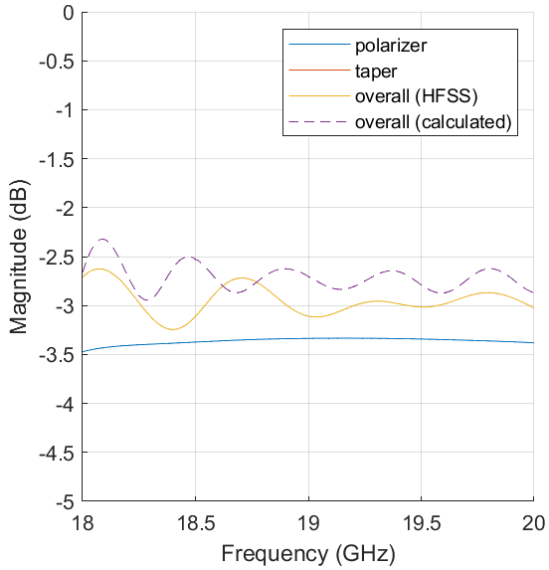

(a) x-polarized mode

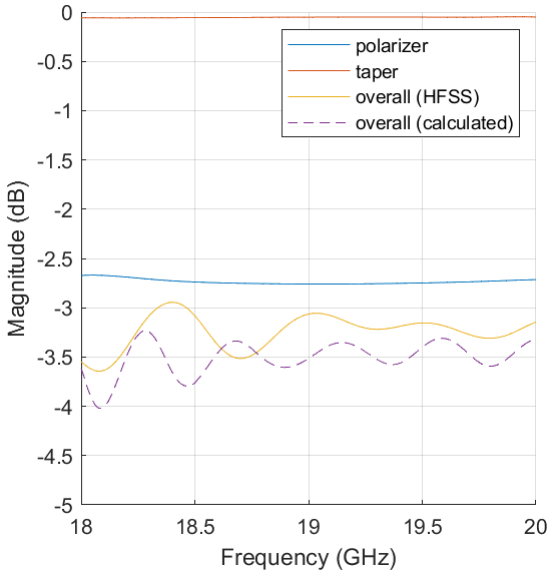

(b) y-polarized mode

FIG. 18: S_{21} of both components in series

subject to a circularly polarized incident waves, as in the actual CRES process. Furthermore, it provides an accessible example to compare the 4-port network cascading described in Section III E to HFSS results. We begin by examining the system with linearly polarized TE_{11} modes inputted at the circular waveguide. Then, we simulate a circularly polarized wave at the input by superimposing x- and y-polarized modes with a 90 degree phase shift.

We observe that both the x and y polarization inputted into the combined system transmit -3 dB into the rectangular TE_{10} mode, or half-power (Fig. 18). Likewise, both polarizations see about -6 dB reflected into themselves, about 1/4 power (Fig. 17). Intuitively, the polarizer transforms a linearly polarized wave into a circularly polarized wave, which is a superposition of an x- and y-polarized wave with equal magnitude. The y-polarized component transmits, and the x-polarized component reflects off the waveguide taper. Half of the reflected component appears in the x-polarized mode and half of it appears in the y-polarized mode at the input. Additionally, the HFSS numerical simulations are closely approximated by the 4-port cascaded S-parameters (dashed lines).

By combining the S-parameters with a $\pi/2$ phase shift ($\pm i$), we can simulate the performance under a circularly polarized wave.

$$\text{Active } S_{ij} = \frac{E_x S_{ij,x} + E_y S_{ij,y}}{|E_x|^2 + |E_y|^2} = \frac{S_{ij,x} \pm i S_{ij,y}}{\sqrt{2}} \quad (18)$$

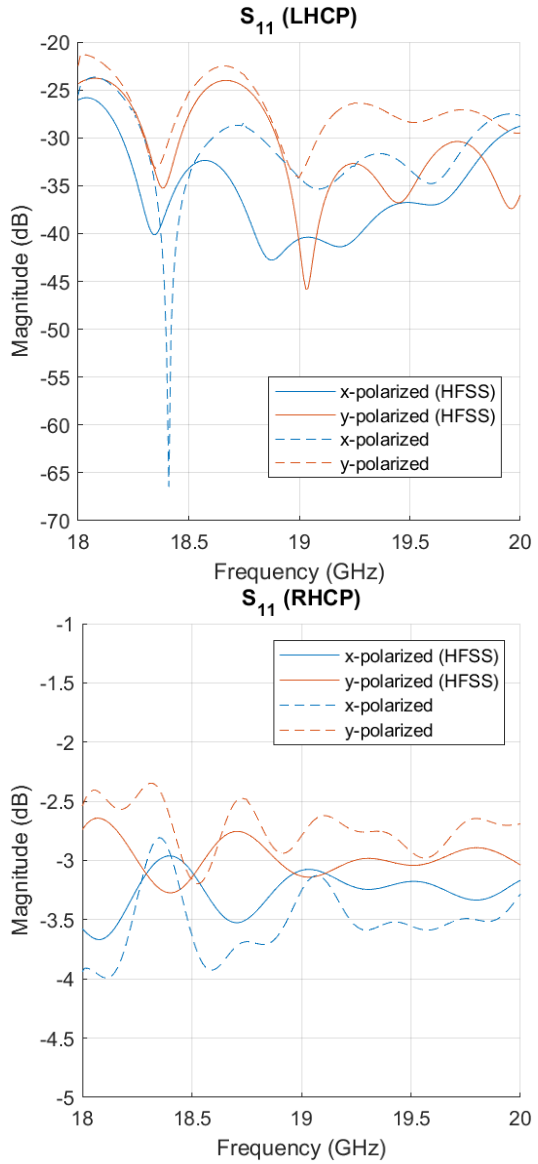

FIG. 19: Active S_{11} of a LHCP (top) and RHCP (bottom) wave

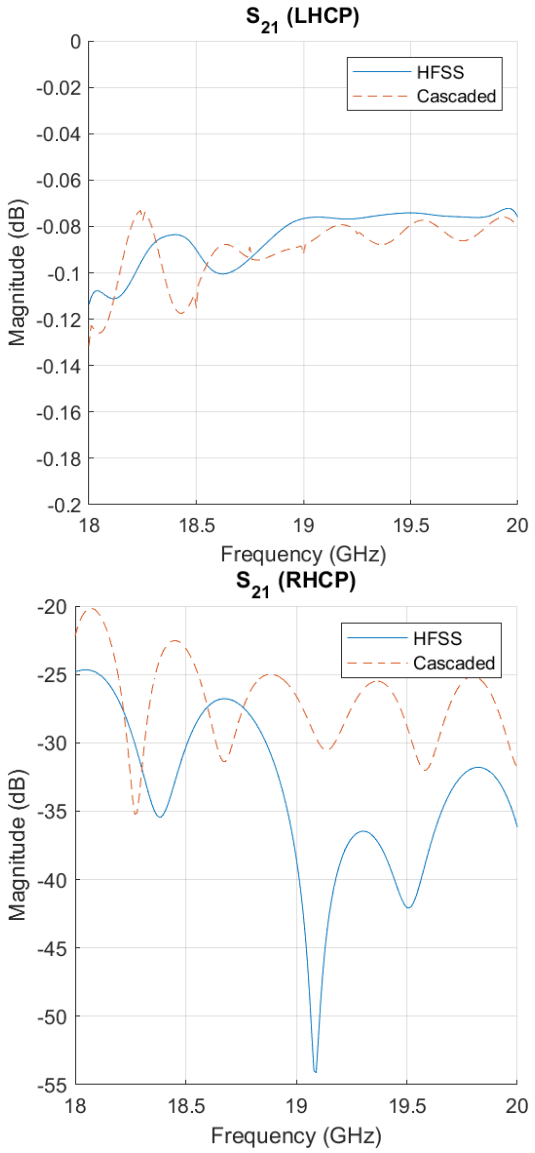

FIG. 20: Active S_{21} of a LHCP (top) and RHCP (bottom) wave

The HFSS model of the polarizer-taper assembly is oriented to transmit left-hand circularly polarized (LHCP) waves and reflect right-hand circularly polarized (RHCP) waves. In Figure 19, we can observe that the Active S_{11} is very low (< -20 dB into each polarization) for a LHCP wave, much better than the -6 dB result for linearly polarized input waves. We also see that -3 dB (half power) of an incident RHCP wave is reflected into each polarization, so all the power is reflected.

The transmission into the rectangular guide propagating mode (S_{21}) of a LHCP wave is nearly 0 dB (Fig. 20), even better than the -3 dB transmission observed with linearly polarized input waves. We also see that < -20 dB of the power in a RHCP wave transmits.

VI. CONCLUSION

The He6-CRES experiment is looking for signatures of non-standard nuclear interactions in the ^{6}He and ^{19}Ne β spectra, using a novel experimental technique that measures the cyclotron radiation frequency of individual $\beta^{\pm}$ particles. We are investigating frequency-dependent oscillations in the signal-to-noise ratio of the system which may be explained by reflections in the system causing a Fabry-Pérot effect. Characterizing the RF behavior of individual components in the experiment's RF system is important for building an accurate model of reflections in the apparatus; this paper presents Ansys HFSS simulations of two key components: the quarter-wave polarizer and circular-to-rectangular waveguide transition. We show that under a circularly polarized incident wave, a

properly aligned quarter-wave polarizer transmits no less than -0.12 dB into a rectangular waveguide TE_{10} mode and reflects no more than -20 dB. This is significantly better performance than under a pure linearly polarized incident wave.

When cascading the polarizer and waveguide transition in series, we present the HFSS simulated S-parameters alongside values calculated from the invididual component S-parameters using Transfer S-parameters, or T-parameters. Despite some error, possibly attributable to mesh variation between simulations and other numerical artifacts, the T-parameter approach broadly reproduces simulation results in order of magnitude and key features. This result suggests using T-parameters to cascade individually simulated components as a viable alternative to performing computationally expensive simulations of larger sections of the apparatus for the purpose of generally modeling the oscillations.

Further work remains to produce a simulation of the Phase II circular waveguide terminator. Ultimately, with accurate simulation of the terminator and decay cell, this analysis will aim to produce a full model of the He6-CRES RF system and to reproduce oscillations in the signal transmitted from the decay cell to the LNA output. Such an analysis will be used to correct the observed SNR oscillations in future upgrades, allowing for better precision and higher sensitivity to new physics.

[1] W. Byron, H. Harrington, R. J. Taylor, W. DeGraw, N. Buzinsky, B. Dodson, M. Fertl, A. García, G. Garvey, B. Graner, M. Guigue, L. Hayen, X. Huyan, K. S. Khaw, K. Knutsen, D. McClain, D. Melconian, P. Müller, E. Novitski, N. S. Oblath, R. G. H. Robertson, G. Rybka, G. Savard, E. Smith, D. D. Stancil, M. Sternberg, D. W. Storm, H. E. Swanson, J. R. Tedeschi, B. A. VanDevender, F. E. Wietfeldt, A. R. Young, and X. Zhu (He6-CRES Collaboration), First observation of cyclotron radiation from MeV-scale $e^{\pm}$ following nuclear β decay, Phys. Rev. Lett. **131**, 082502 (2023).

[2] H. Saul, C. Roick, H. Abele, H. Mest, M. Klopf, A. K. Petukhov, T. Soldner, X. Wang, D. Werder, and B. Märkisch, Limit on the Fierz interference term b from a measurement of the beta asymmetry in neutron decay, Phys. Rev. Lett. **125**, 112501 (2020).

[3] B. Monreal and J. A. Formaggio, Relativistic cyclotron radiation detection of tritium decay electrons as a new technique for measuring the neutrino mass, Phys. Rev. D **80**, 051301 (2009).

[4] D. M. Asner, R. F. Bradley, L. de Viveiros, P. J. Doe, J. L. Fernandes, M. Fertl, E. C. Finn, J. A. Formaggio, D. Furse, A. M. Jones, J. N. Kofron, B. H. LaRoque, M. Leber, E. L. McBride, M. L. Miller, P. Mohanmurthy, B. Monreal, N. S. Oblath, R. G. H. Robertson, L. J. Rosenberg, G. Rybka, D. Rysewyk, M. G. Sternberg, J. R. Tedeschi, T. Thümmler, B. A. VanDevender, and N. L. Woods (Project 8 Collaboration), Single-electron detection and spectroscopy via relativistic cyclotron radiation, Phys. Rev. Lett. **114**, 162501 (2015).

[5] C. Weinheimer, KATRIN, a next generation tritium β decay experiment in search for the absolute neutrino mass scale, Progress in Particle and Nuclear Physics **48**, 141 (2002).

[6] J. Jackson, *Classical Electrodynamics*, 3rd ed. (John Wiley & Sons, 1999).

[7] D. M. Pozar, *Microwave Engineering*, 4th ed. (Wiley, Hoboken, NJ, 2012).

[8] N. Buzinsky, Reflections in He6-CRES (2023), (Internal Report).

[9] N. Buzinsky, N-Mirror Fabry-Pérot Cavity (2023), (Internal Report).

[10] ProofWiki, Neumann Series Theorem, URL `https://proofwiki.org/wiki/Neumann_Series_Theorem`.

[11] J. Frei, X.-D. Cai, and S. Muller, Multiport S -Parameter and T -Parameter Conversion With Symmetry Extension, IEEE Transactions on Microwave Theory and Techniques **56**, 2493 (2008).

[12] T. Reveyrand, Multiport conversions between S, Z, Y, h, ABCD, and T parameters, in *2018 International Workshop on Integrated Nonlinear Microwave and Millimetre-wave Circuits (INMMIC)* (IEEE, Brive La Gaillarde, 2018).

[13] L. Malavasi, Modeling a Quarter Wave Plate in a Circular Waveguide with Ansys HFSS (2023), (Internal Report).